

<sup>1</sup> To the Graduate Council:  
<sup>2</sup> I am submitting herewith a thesis written by Jason Bane entitled “The EMC Effect  
<sup>3</sup> in A=3 Nuclei.” I have examined the final paper copy of this thesis for form and  
<sup>4</sup> content and recommend that it be accepted in partial fulfillment of the requirements  
<sup>5</sup> for the degree of Doctor of Philosophy, with a major in Nuclear Physics.

<sup>6</sup>  
<sup>7</sup>

---

Nadia Fomin, Major Professor

<sup>8</sup> We have read this thesis  
<sup>9</sup> and recommend its acceptance:

<sup>10</sup> \_\_\_\_\_

<sup>11</sup> Jamie Coble

<sup>12</sup> \_\_\_\_\_

<sup>13</sup> Kate Jones

<sup>14</sup> \_\_\_\_\_

<sup>15</sup> Thomas Papenbrock

<sup>16</sup> \_\_\_\_\_

<sup>17</sup> Soren Soreson

<sup>18</sup>

Accepted for the Council:

<sup>19</sup>  
<sup>20</sup>

---

Carolyn R. Hodges

<sup>21</sup>

Vice Provost and Dean of the Graduate School

<sup>22</sup> To the Graduate Council:  
<sup>23</sup> I am submitting herewith a thesis written by Jason Bane entitled “The EMC Effect  
<sup>24</sup> in A=3 Nuclei.” I have examined the final electronic copy of this thesis for form and  
<sup>25</sup> content and recommend that it be accepted in partial fulfillment of the requirements  
<sup>26</sup> for the degree of Doctor of Philosophy, with a major in Nuclear Physics.

<sup>27</sup> Nadia Fomin, Major Professor

<sup>28</sup> We have read this thesis  
<sup>29</sup> and recommend its acceptance:

<sup>30</sup> Jamie Coble

<sup>31</sup> \_\_\_\_\_  
<sup>32</sup>

<sup>33</sup> Kate Jones

<sup>34</sup> \_\_\_\_\_  
<sup>35</sup>

<sup>36</sup> Thomas Papenbrock

<sup>37</sup> \_\_\_\_\_  
<sup>38</sup>

<sup>39</sup> Soren Soreson

<sup>40</sup> \_\_\_\_\_  
<sup>41</sup>

<sup>42</sup> Accepted for the Council:

<sup>43</sup>  
<sup>44</sup> Carolyn R. Hodges

<sup>45</sup> \_\_\_\_\_  
<sup>46</sup>

<sup>47</sup> Vice Provost and Dean of the Graduate School

<sup>48</sup> (Original signatures are on file with official student records.)

49

# The EMC Effect in A=3 Nuclei

50

A Thesis Presented for

51

The Doctor of Philosophy

52

Degree

53

The University of Tennessee, Knoxville

54

Jason Bane

55

December 2018

<sup>56</sup>

© by Jason Bane, 2018

<sup>57</sup>

All Rights Reserved.

# <sup>58</sup> Contents

<sup>59</sup>	<b>List of Tables</b>	<b>v</b>
<sup>60</sup>	<b>List of Figures</b>	<b>vi</b>
<sup>61</sup>	<b>1 Introduction</b>	<b>1</b>
<sup>62</sup>	1.1 Electron scattering . . . . .	2
<sup>63</sup>	1.1.1 Deep inelastic scattering . . . . .	5
<sup>64</sup>	1.2 EMC Effect . . . . .	6
<sup>65</sup>	1.3 MARATHON . . . . .	9
<sup>66</sup>	<b>2 Experimental Setup</b>	<b>10</b>
<sup>67</sup>	2.1 Thomas Jefferson Lab . . . . .	10
<sup>68</sup>	2.1.1 CEBAF . . . . .	10
<sup>69</sup>	2.1.2 Hall A . . . . .	12
<sup>70</sup>	2.2 Target . . . . .	17
<sup>71</sup>	2.3 High Resolution Spectrometers . . . . .	19
<sup>72</sup>	2.3.1 Vertical Drift Chambers . . . . .	20
<sup>73</sup>	2.3.2 Scintillators . . . . .	22
<sup>74</sup>	2.3.3 Cherenkov . . . . .	22
<sup>75</sup>	2.3.4 Shower Calorimeter . . . . .	22
<sup>76</sup>	2.3.5 Pion Rejector . . . . .	22
<sup>77</sup>	2.3.6 FPP Chambers . . . . .	22

78	2.4 Trigger Setup . . . . .	22
79	2.5 DAQ - Data Acquisition System . . . . .	22
80	2.6 Kinematic Settings . . . . .	22
81	<b>3 Calibration</b>	<b>23</b>
82	3.1 Beam Line . . . . .	23
83	<b>4 Data Analysis</b>	<b>26</b>
84	<b>5 Results</b>	<b>27</b>
85	<b>6 Simulation</b>	<b>28</b>
86	6.1 Investigation . . . . .	28
87	6.2 Transformation . . . . .	29
88	6.3 Results . . . . .	31
89	<b>7 Conclusion</b>	<b>34</b>
90	<b>Bibliography</b>	<b>35</b>

<sub>91</sub> **List of Tables**

# <sub>92</sub> List of Figures

<sub>93</sub>	1.1	Simple Feynman diagram of an electron scattering from a proton [7].	3
<sub>94</sub>	1.2	Graph of the ratio of A/D structure functions vs $x$ for Carbon [10]. . . . .	7
<sub>95</sub>	1.3	EMC effect from EMC, SLAC, and BCDMS [17] . . . . .	8
<sub>96</sub>	1.4	Graph of the ratio of A/D structure functions vs $x$ for Carbon [10]. . . . .	9
<sub>97</sub>	2.1	Schematic Layout of CEBAF. . . . .	11
<sub>98</sub>	2.2	A 3D drawing of Hall A. . . . .	12
<sub>99</sub>	2.3	A schematic layout of the beam line in Hall. [1] . . . . .	13
<sub>100</sub>	2.4	BPM design diagram, from JLab instrumentation group. Beam direction is from left to right [23]. . . . .	14
<sub>102</sub>	2.5	BPM design diagram, looking down the beam line[23]. . . . .	14
<sub>103</sub>	2.6	Hall A Current Monitor components [4]. . . . .	16
<sub>104</sub>	2.7	Target Images . . . . .	18
<sub>105</sub>	2.8	A side view of a HRS [1]. . . . .	20
<sub>106</sub>	2.9	A view of both the left(top) and right(bottom) detector stacks inside the left and right HRS [1]. . . . .	21
<sub>108</sub>	2.10	A sketch of the two VDC planes in the HRSs with a particle traveling through the detector at $45^\circ$ .[6]. . . . .	22
<sub>110</sub>	3.1	A schematic layout of a harp fork [23] . . . . .	24
<sub>111</sub>	3.2	The X and Y position for a Bulls eye scan for BPM calibration. . . . .	25

112	6.1 Example of the electron beam(red) with a energy of 2.5 GeV and the	
113	proton(blue) with angle of 45° in respect to the electron and with a	
114	momentum of 0.5 GeV/c. . . . .	29
115	6.2 Vector representations of the momentum for the incoming electron(red)	
116	and target proton(blue) with units of GeV for each phase of their	
117	transformations before scattering. . . . .	30
118	6.3 Vector representations of the momentum for the incoming electron(red)	
119	and target proton(blue) with units of GeV for each phase of their	
120	transformations after scattering). . . . .	32
121	6.4 Simulation results for fixed momentum protons. Three runs with	
122	unique proton momentum. . . . .	33

<sup>123</sup> **Chapter 1**

<sup>124</sup> **Introduction**

<sup>125</sup> Understanding the world around us is the goal of every scientist, from the chemist  
<sup>126</sup> that experiments with the formation of atoms to the geologist exploring the process of  
<sup>127</sup> rock formations. Nuclear physicists focus on studying the fundamental constituents  
<sup>128</sup> of matter, the building blocks of nature. Physicist use scattering experiments at  
<sup>129</sup> accelerator facilities, like CERN in Switzerland, DESY in Germany, BATES in  
<sup>130</sup> Massachusetts, JLAB in Virginia, and many others, to study the protons and neutrons  
<sup>131</sup> and their constituents that make up a nucleus. These experiments allow physicists  
<sup>132</sup> to observe the internal structure of the nucleus and to investigate the interactions  
<sup>133</sup> between the quarks and gluons. Many of the experiments are design to confirm a  
<sup>134</sup> existing results while also expanding on unique ideas.

<sup>135</sup> In the last century, there have been numerous breakthroughs in the fields of nuclear  
<sup>136</sup> and particle physics. Rutherford discovered the proton by bombarding light nuclei  
<sup>137</sup> with alpha particles to produce



<sup>138</sup> This reaction allowed Rutherford to conclude that the Hydrogen nucleus was a  
<sup>139</sup> constituent of an atomic nuclei [18]. In the late 1950s, experimental results published

140 by W. McAllister and R. Hofstadter exposed some of the eternal structure of the  
141 proton [7, 15]. The European Muon Collaboration(EMC) produced results in the  
142 early 1980s showing a differences between the internal structure of the deuterium  
143 nucleus and Iron [20, 10]. The data received from scattering experiments using alpha  
144 particles contain information about the target, the beam, and the interaction between  
145 the two. Deciphering and analyzing this data can be convoluted because the cross-  
146 section contains information about the internal structure of the target and the beam  
147 along with the interaction and forces between the two [18].

## 148 1.1 Electron scattering

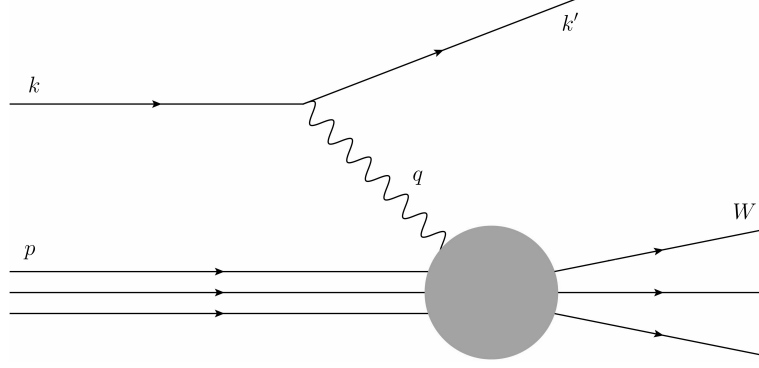
149 In order to remove some of the complexity in scattering experiments, one may  
150 employ highly relativistic electrons. Electrons being point-like particles without any  
151 internal structure allow the elimination of some of the analysis difficulties with using  
152 alpha particles in scattering experiments due to their complex internal structure.  
153 Electrons and the target nucleus, nucleon, or quarks interact via the exchange of  
154 a virtual photon. Using quantum electrodynamics (QED), these interactions can  
155 accurately be described by the well known electromagnetic interaction. Higher order  
156 terms of this process contribute very little due to the coupling constant  $\alpha \approx 1/137$ ,  
157 being much smaller than one.

158 Figure 1.1 represents an electron scattering from a proton. The incoming or incident  
159 electron's four-momentum is described as  $k = (E, \vec{k})$  and the scattering electron's four-  
160 momentum is represented by  $k' = (E', \vec{k}')$ . The exchange of the virtual photon in this  
161 electromagnetic interaction is defined by the four-momentum transfer  $q$ :

$$Q^2 \equiv -q^2 = 4EE' \sin^2(\theta/2). \quad (1.2)$$

<sub>162</sub> In equation 1.2, E and E' are the electron energy before and after the scattering  
<sub>163</sub> interaction. Theta is the angle that describes the deflection of E' from the electron's  
<sub>164</sub> original path.

**Figure 1.1:** Simple Feynman diagram of an electron scattering from a proton [7].



<sub>165</sub> Along with  $Q^2$ , the variables  $\nu$ ,  $W$ , and  $x_B$  are used to narrate the evolution of the  
<sub>166</sub> electron scattering process.  $\nu$ , defined as  $p \cdot q/M$ . In the rest frame of the target,  $\nu$   
<sub>167</sub> can be described by:

$$\nu = E - E'. \quad (1.3)$$

<sub>168</sub> Simply,  $\nu$  is the magnitude of energy loss by the electron during the scattering  
<sub>169</sub> interaction. The invariant mass of the system,  $W$ , defines the hadronic state produced  
<sub>170</sub> by the scattering event.

$$W^2 \equiv (q + p)^2 = M^2 + 2M\nu - Q^2. \quad (1.4)$$

<sub>171</sub> A scattering event with the invariant mass equal to the square of the mass of the  
<sub>172</sub> nucleon, ( $M^2$ ), falls in the regime of elastic scattering.  $W$  above  $M^2$  will transform  
<sub>173</sub> the scattering interaction from an elastic scattering to inelastic scattering due to  
<sub>174</sub> the excited state of the scattered byproduct.  $x_B$ , the Bjorken scaling variable is a  
<sub>175</sub> dimensionless quantity that measures the inelasticity of a scattering process.  $x_B$  is  
<sub>176</sub> defined as:  $x := \frac{Q^2}{2M\nu}$ .

177      The intrinsic likelihood of an event with a certain  $Q^2$ ,  $\nu$ , and  $W$  is defined by the  
 178   scattering cross section. An electron scattering off of a target with a charge of  $Z * e$   
 179   can be described by the Rutherford cross-section. Povh et. al. details the Rutherford  
 180   cross section as:

$$\left( \frac{d\sigma}{d\Omega} \right)_{Rutherford} = \frac{(zZe^2)^2}{(4\pi\epsilon_0)^2 * (eE_{kin})^2 \sin^4(\theta/2)}. \quad (1.5)$$

181   In the early 1920s, German physicists Stern and Gerlach performed an experiment  
 182   that confirmed the presence of electron angular momentum. Later a discovery of  
 183   electron spin was made by Uhlenbeck and Goudsmit. The Rutherford cross-section  
 184   neglects the spin of an electron and its target. The Mott cross-section is the evolved  
 185   version of the Rutherford cross-section. It has been modified to include the intrinsic  
 186   spin of the target and electron. The Mott cross-section is: [12, 18]

$$\left( \frac{d\sigma}{d\Omega} \right)_{Mott} = \frac{4Z^2\alpha^2(\hbar c)^2 E'^2}{|\mathbf{q}_c|^4} \cos^2(\theta/2). \quad (1.6)$$

187   There is an agreement between the measured cross section and the theoretical Mott  
 188   cross-section when in the limit of  $|\mathbf{q}| \rightarrow 0$  for scattering events of electrons off of a  
 189   target nuclei. As  $|\mathbf{q}|$  climbs further from zero, the experimentally measured cross  
 190   sections systematically decreases [18]. Increasing the  $|\mathbf{q}|$  of an interaction reduces  
 191   the size of the wavelength of the virtual photon that mediates the electromagnetic  
 192   interaction between the electron and target nuclei and increases the resolution of the  
 193   probe. The wavelength of this virtual photon is inversely proportional to  $|\mathbf{q}|$ , and can  
 194   be described by the following:  $\lambda = \frac{\hbar}{|\mathbf{q}|}$  [18]. Increasing the amount of momentum  
 195   transferred in an electromagnetic reaction allows one to study deeper into the nucleus.

196   Studying the internal structure of a nucleus with the electromagnetic interaction  
 197   requires increasing the momentum transferred. Pushing  $|\mathbf{q}|$  to be comparable with the  
 198   mass of a nucleon adds more complexity to the details of the scattering interaction.

199 At the appropriate levels of  $|\mathbf{q}|$  to study the nucleons in the nucleus, the Mott cross-  
 200 section equation requires modifications to include additional factors that incorporate  
 201 information about the target. The Rosenbluth formula is based on the Mott  
 202 cross section and embraces target recoil, magnetic moment, and charge and current  
 203 distributions. Povh writes the Rosenbluth formula as:

$$\left(\frac{d\sigma}{d\Omega}\right) = \left(\frac{d\sigma}{d\Omega}\right)_{Mott} * \left[ \frac{G_E^2(Q^2) + \tau G_M^2(Q^2)}{1 + \tau} + 2\tau G_M^2(Q^2) \tan^2 \frac{\theta}{2} \right]. \quad (1.7)$$

204 Equation 1.7 contains  $G_E^2(Q^2)$  and  $G_M^2(Q^2)$ , the electric and magnetic form factors.  $\tau$   
 205 is used in the Rosenbluth formalism to account for the magnetic moment of a nucleon  
 206 and is defined as:  $\tau = \frac{Q^2}{4M^2c^2}$  [18]. In the general case of electron scattering off of a free  
 207 proton or neutron elastically, the scattered energy of the electron will be a function  
 208 of the incident electron's energy and the scattered angle of the electron, shown in the  
 209 following equation.

$$E' = \frac{E}{1 + \frac{E}{Mc^2}(1 - \cos\theta)} \quad (1.8)$$

### 210 1.1.1 Deep inelastic scattering

211 The first generation of electron scattering experiments achieving a significantly  
 212 large  $|\mathbf{q}|$  used a linear accelerator with a 25 GeV maximum beam energy, and  
 213 following generations increased the total interaction energy to substantially higher  
 214 thresholds. At these high incident beam energies, individual resonances cannot be  
 215 separated in the invariant mass spectrum above 2.5 GeV. Observations made into  
 216 this convoluted invariant mass spectrum has shown that many strongly interacting  
 217 particles are produced, known as hadrons. Scattering interactions that generate  
 218 these hadrons are considered to be inelastic. Inelastic scattering events contain  
 219 the possibility of conceiving additional resultants and increase the complexity of  
 220 a scattering interaction. Inelastic scattering events occur when the wavelength  
 221 of the virtual photon is comparable to the radius of the struck nucleon or when  
 222  $Q^2 R^2 \lesssim 1$  [18]. Increasing the amount of transferred momentum so that  $Q^2 R^2 \gtrsim 1$ ,

223 increase the resolution of the probe to a level that allows for the interacting with  
 224 the charge constituents within the nucleon. When the scattering event probes the  
 225 fundamental elements of a nucleon, the scattering process is titled deep inelastic  
 226 scattering(DIS). Due to the increase in complexity, an additional degree of freedom  
 227 has to be introduced into the scattering cross section equation. Modifying the  
 228 Rosenbluth formula to include the inelastic scattering structure functions  $F_1(Q^2, \nu)$   
 229 and  $F_2(Q^2, \nu)$  evolves the Rosenbluth formula to contain the needed complexity of an  
 230 inelastic event. These modifications are shown in equation 1.9.

$$\frac{d^2\sigma}{d\Omega dE'} = \left( \frac{d\sigma}{d\Omega} \right)_{Mott} \left[ \frac{F_2(Q^2, \nu)}{\nu} + \frac{2F_1(Q^2, \nu)}{M} \tan^2 \frac{\theta}{2} \right] \quad (1.9)$$

231 The  $F_1$  and  $F_2$  structure functions provide the details for describing the internal  
 232 composition of the nucleon [18].

$$F_2(x) = x \mathbf{1} \cdot \sum_f z_f^2 (q_f(x) + \bar{q}_f(x)) \quad (1.10)$$

233 [21] [13]

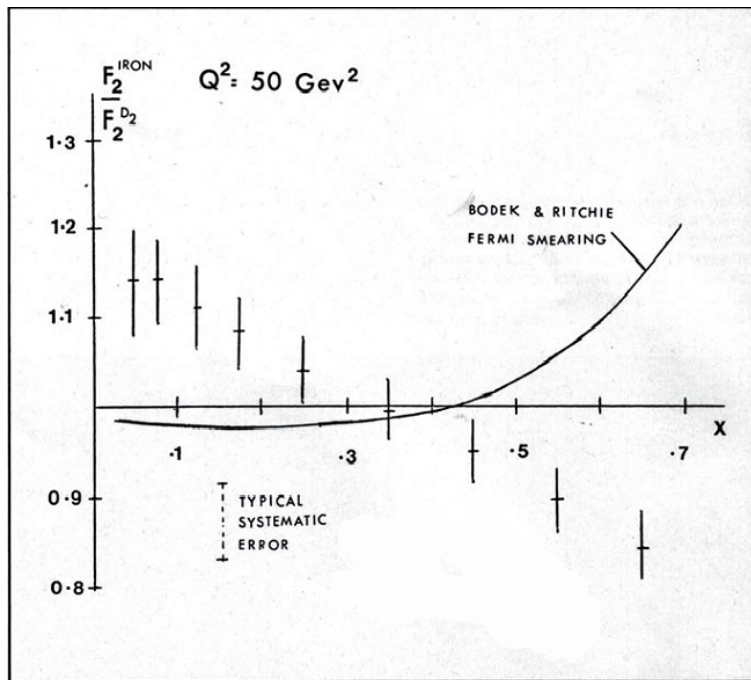
## 234 1.2 EMC Effect

235 The European Muon Collaboration (EMC) performed a deep inelastic measurement  
 236 with 120-280 GeV muons on iron and deuteron targets [14]. The EMC extracted A/D  
 237 structure function ratios versus the Bjorken scaling variable,  $x$ . The relationship  
 238 originally expected by the EMC contained the sum of the structure functions of each  
 239 nucleon in a nucleus. Each nucleus has a certain number of neutrons ( $N$ ) and a amount  
 240 of protons ( $Z$ ). The expected structure function for a nucleus could be written as:

$$F_A = N F_2^N + Z F_2^P. \quad (1.11)$$

241 The EMC compared the extracted structure functions from iron and deuterium.  
 242 Their results are shown in Figure 1.2. The  $\frac{A}{D}$  structure function ratio showed  
 243 an unexpected downward slope. This phenomenon was titled the EMC effect.  
 244 This finding demonstrated to the EMC that their understanding of the nucleus  
 245 was incorrect. A nucleon's structure function and thereby, the constituent quark  
 distributions may be altered by the nucleus.

**Figure 1.2:** Graph of the ratio of A/D structure functions vs  $x$  for Carbon [10].

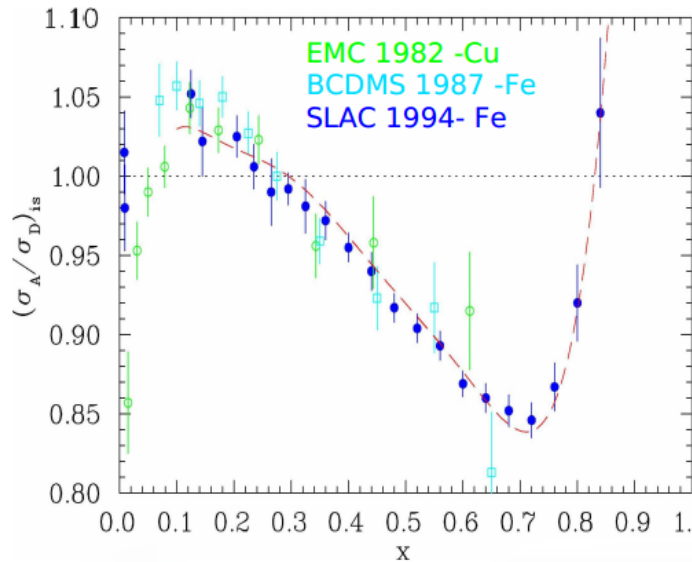


246

247 Ever since the European Muon Collaboration discovered the depletion of quarks at  
 248 high  $x$  for  $A > 2$  nuclei, physicists have tried to discover its cause. Scientists at SLAC  
 249 extracted structure function ratios for many nuclei including;  ${}^4\text{He}$ ,  ${}^9\text{Be}$ ,  ${}^{12}\text{C}$ ,  ${}^{27}\text{Al}$ ,  
 250  ${}^{40}\text{Ca}$ ,  ${}^{56}\text{Fe}$ ,  ${}^{108}\text{Ag}$ , and  ${}^{197}\text{Au}$ . There were slightly different results for each nucleus.  
 251 The magnitude of the EMC effect, taken to be the A/D ratio at  $x = 0.6$ , was found  
 252 to be different for the various nuclei, and roughly scaled with the size or density of  
 253 the nuclei. The NMC (New Muon collaboration), another group at CERN, gathered  
 254 precise data in order to construct the inclusive cross section of deuterium and protons.

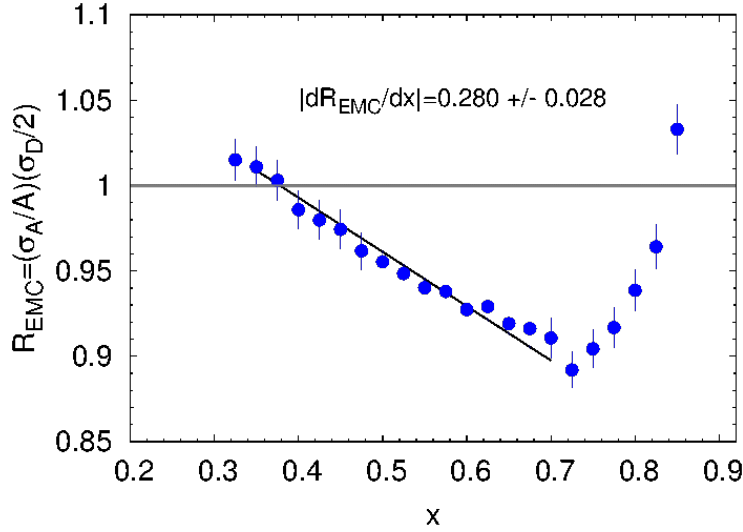
255 BCDMS collaboration extracted data for N and Fe structure function ratios. Figure  
 256 1.3 shows some of the data from SLAC and BCDMS on the EMC effect for Iron  
 257 and Cu. Figure 1.4 shows this result from a recent JLab EMC measurement, most  
 258 precise to date. Many models over the years have been able to reproduce the shape  
 259 of the A/D ratios. These models can contain traditional nuclear physics effects like  
 260 momentum distribution or pion-charge contributions. Some models also describe the  
 261 EMC effect through quark momentum distribution or modification of the internal  
 262 structure [17, 5, 2, 8, 9]. However, no single model has provided a complete picture  
 263 of the possible underlying physics. Precise data from Jlab's E03-103 experiment has  
 264 revitalized this research. This experiment focused on precision measurements in light  
 265 nuclei and added  ${}^3\text{He}$  as a target nucleus. Instead of taking the A/D ratio at a  
 266 certain  $x$ -value to be the magnitude of the EMC effect, this analysis looked at the  
 267 slope instead. This eliminated sensitivity to normalization uncertainties.

**Figure 1.3:** EMC effect from EMC, SLAC, and BCDMS [17]



268 In Figure ,  ${}^9\text{Be}$  was found not to follow the previously observed scaling with  
 269 nuclear density. This result from Jefferson Lab determined that the previous idea

**Figure 1.4:** Graph of the ratio of A/D structure functions vs  $x$  for Carbon [10].



of a dependence on A or nuclear density in the EMC effect to be incorrect [20]. This result spawned a drive to determine another explanation for the EMC effect and understand what clue the  ${}^9\text{Be}$  outlier was providing. The structure of this nucleus is made up of two high-density alpha particles and a single neutron [3]. The regions of higher density that are contained in a comparatively large volume may be able to explain why  ${}^9\text{Be}$  does not follow the expected trend. This suggests that the EMC effect could be a function of local nuclear density [20].

### 1.3 MARATHON

Experiment E12-010-102, MARATHON (MeAsurement of the  $F2^n/F_2^p, d/u$  RAtios and A=3 EMC Effect in Deep Inelastic Electron Scattering Off the Tritium and Helium MirOr Nuclei), will use deep inelastic scattering off of the mirror nuclei  ${}^3\text{H}$  and  ${}^3\text{He}$  to measure the EMC effect for both  ${}^3\text{H}$  and  ${}^3\text{He}$ , to determine the ratio of the neutron to proton inelastic structure functions, and to find the ratio of the down to up quark distributions in the nucleon.

<sup>284</sup> **Chapter 2**

<sup>285</sup> **Experimental Setup**

<sup>286</sup> **2.1 Thomas Jefferson Lab**

<sup>287</sup> Thomas Jefferson Lab (Jlab) in Newport News, Virginia hosted the MARATHON  
<sup>288</sup> experiment in the Fall of 2017 and Spring of 2018. Jlab uses support from the U.S.  
<sup>289</sup> Department of Energy(DOE) and the state of Virgina to complete the lab's mission of  
<sup>290</sup> delivering productive research by exploring the atomic nucleus and its fundamental  
<sup>291</sup> constituents, including precise tests of their interactions. Along with applying an  
<sup>292</sup> advanced particle accelerator, particle detectors and other technologies to develop  
<sup>293</sup> new basic research capabilities and to address the challenges of a modern society.

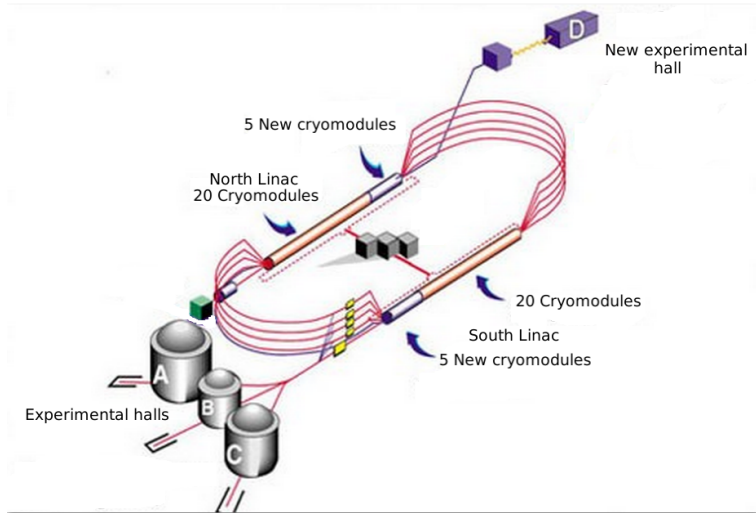
<sup>294</sup> **2.1.1 CEBAF**

<sup>295</sup> The Continuous Electron Beam Accelerator Facility (CEBAF) was recently  
<sup>296</sup> upgraded to a 12 GeV accelerator, upgrading it to be able to supply a 11 GeV beam  
<sup>297</sup> of continuous electrons of up to  $200 \mu\text{A}$  of current to three experimental halls (A,B,C)  
<sup>298</sup> and 12 GeV to the recently constructed hall D. After being accelerated to 45 MeV by  
<sup>299</sup> a polarized electron gun or a thermionic injector, the electrons are injected into the  
<sup>300</sup> North linear accelerator (LINAC), shown in figure 2.1. The polarized gun can supply  
<sup>301</sup> electrons with up to 80% polarization and the polarization direction can be controlled

302 by a wien filter. To ensure the level of polarization, a 5 MeV Mott polarimeter may  
303 be used to measure the level of polarization[1].

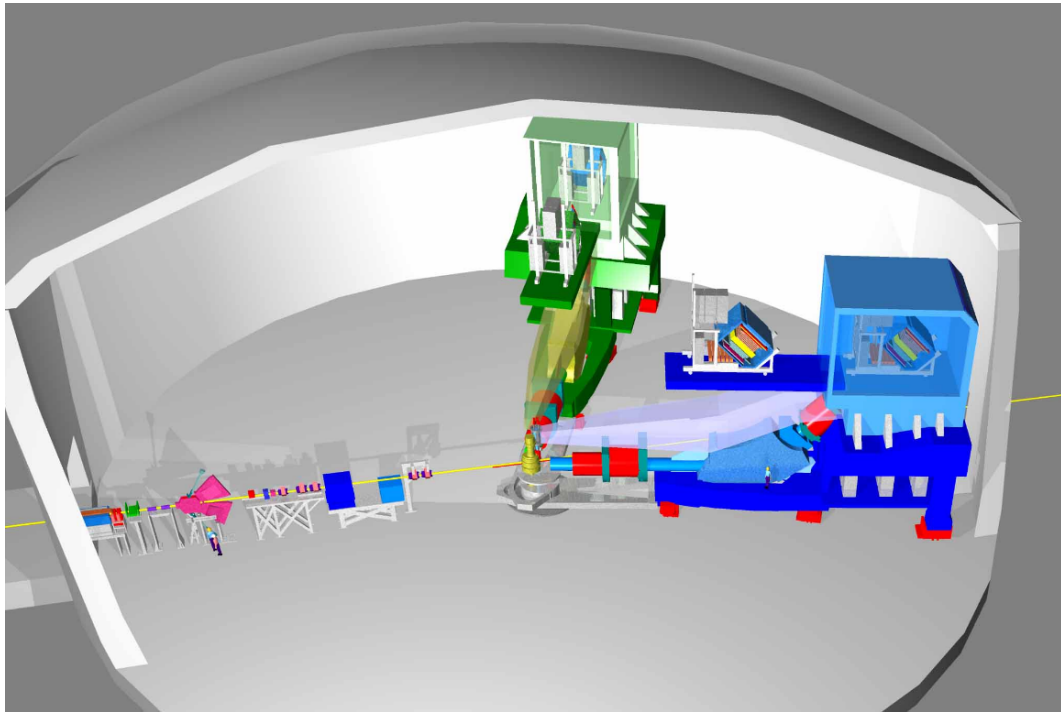
304 The electrons are conveyed through two LINACs and two bending arcs per complete  
305 pass of the accelerator. Electrons traveling to Halls A, B, and C complete a maximum  
306 of four and a half revolutions around the accelerator. Electrons going to all D travel  
307 through the north LINAC for an extra boost. These particles receive approximately  
308 2.2 GeV in energy for each cycle through the accelerator. The radio frequency (RF)  
309 cavities in each LINAC use an oscillating electromagnetic field to supply a force to  
310 accelerate the passing electrons. These Niobium RF cavities are cooled to 2 K in  
311 order to create conditions that allow the cavities to be superconducting [1].

**Figure 2.1:** Schematic Layout of CEBAF.



<sub>312</sub> **2.1.2 Hall A**

**Figure 2.2:** A 3D drawing of Hall A.

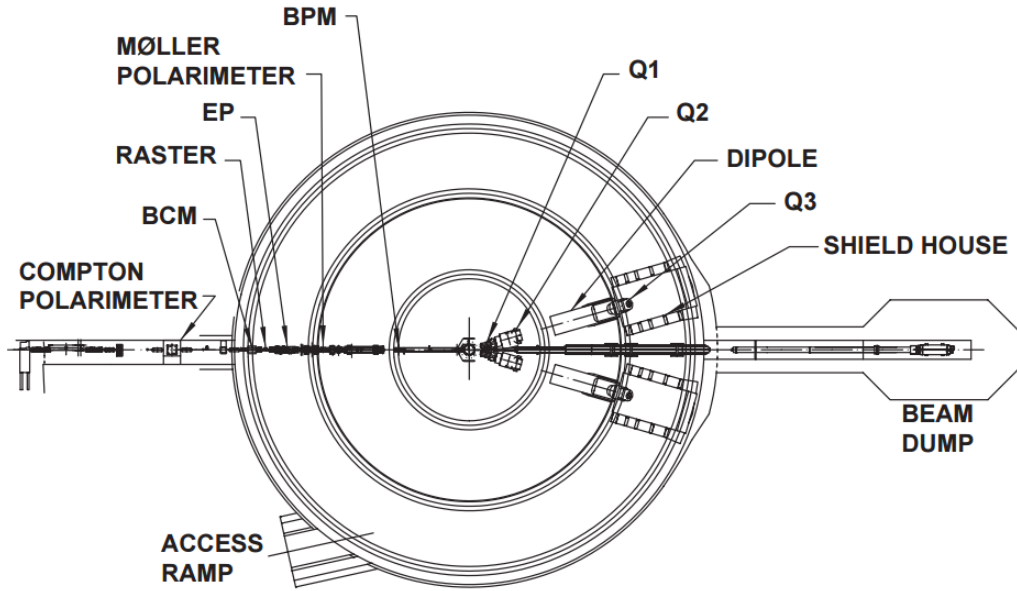


<sub>313</sub> The experimental Hall A and the scientific equipment used were designed for  
<sub>314</sub> detailed investigations of the internal structure of nuclei. Two high resolution  
<sub>315</sub> spectrometers in Hall A use the inclusive ( $e,e'$ ) and exclusive ( $e,e' p$ ) reactions to gain  
<sub>316</sub> a greater understanding of the structure of the nucleus. Completing detailed studies  
<sub>317</sub> with high resolution and extreme accuracy requires knowing the beam position, size,  
<sub>318</sub> energy, current, direction, and polarization when the beam strikes the target. The  
<sub>319</sub> instrumentation used in the precise measurement of these quantities in Hall A are  
<sub>320</sub> shown in figure 2.3 [1].

<sub>321</sub> A pair of Beam Position Monitors(BPM)s are used to measure the relative beam  
<sub>322</sub> position without affecting the beam. The two Hall A BPMs are located at 7.524 m  
<sub>323</sub> and 1.286 m away from the target. Using the standard difference-over-sum technique,  
<sub>324</sub> the relative beam position is determined with an accuracy of 100  $\mu\text{m}$  with a beam

325 current of at least  $1 \mu\text{A}$  [1]. The BPMs' positional data is recorded in two ways.  
 326 Every second of beam time, the beam position average over 0.3 seconds is logged  
 327 into the Experimental Physics and Industrial Control System (EPICS) database.  
 328 The BPMs also transmit data event-by-event to the CEBAF online Data Acquisition  
 329 system(CODA).

**Figure 2.3:** A schematic layout of the beam line in Hall. [1]



330 The main beam line components of the BPMs consist of four open-ended antennas.  
 331 Figure 2.4 shows a BPM chamber and figure 2.5 shows the layout of the four antennas  
 332 as you look down the beam line. In this chamber, the design of three of the four  
 333 antennas can be seen. The antennas are titled  $u_+$ ,  $u_-$  and  $v_+$ ,  $v_-$ . The antennas  
 334 receive an induced signal as electrons pass to determine the beam position in the  
 335 u and v directions. The direction of the beam is determined by using the two  
 336 BPMs in conjunction with timing information provided. The accuracy of the BPMs  
 337 requires an absolute measurement of the electron beam's position to calibrate the  
 338 BPMs and a internal input oscillation measurement names twiddle to supply BPM  
 339 signal coefficients. [19, 23].

**Figure 2.4:** BPM design diagram, from JLab instrumentation group. Beam direction is from left to right [23].

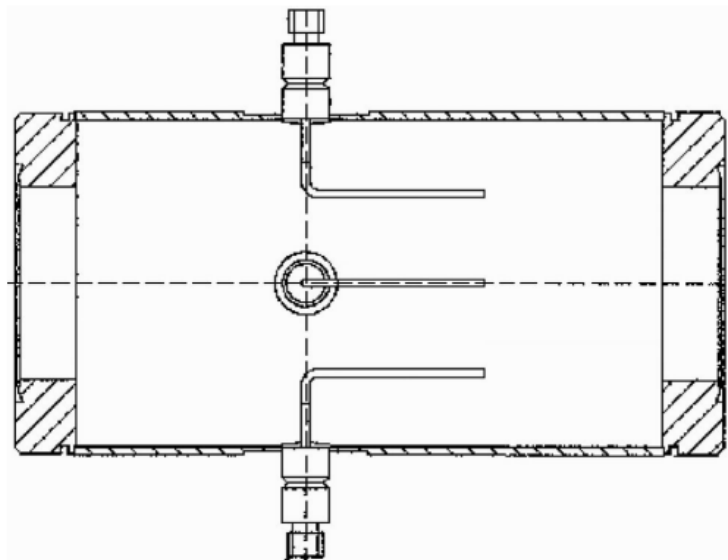
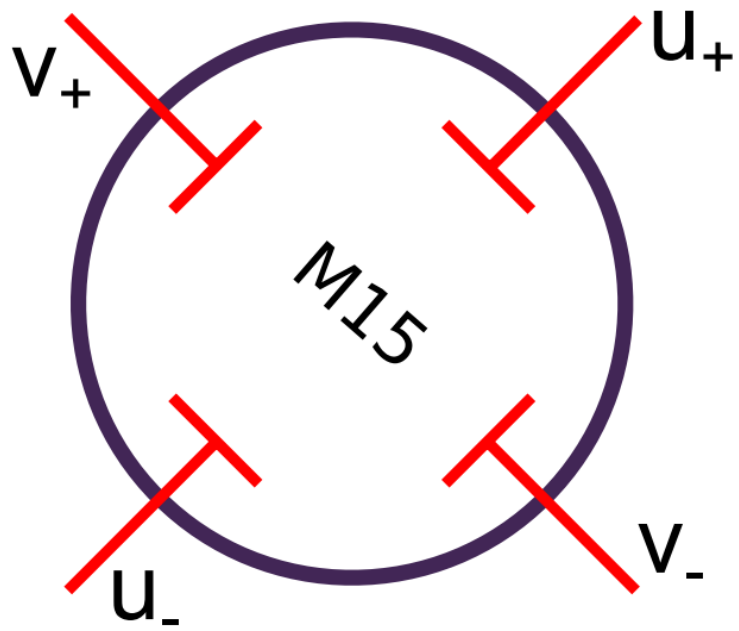


**Figure 2.5:** BPM design diagram, looking down the beam line[23].



340 Damage to a target system from intense beam can cause extreme fluctuations in  
341 the target's temperature and density. A raster was used to counteract the damage

342 caused by a focused beam. The raster used two magnetic fields produced by two  
343 dipoles to spread the electron beam out. This produces a large rectangle interaction  
344 area on the front face of the target container. A triangle wave of 25 kHz was used to  
345 control the coils of the dipole magnets. The raster systems are located  $\approx$ 17 meters  
346 before the target chamber (upstream of the target[23]). The rasters position can be  
347 seen in figure 2.2. Safety constraints administrated by the target group at JLAB  
348 limited the minimum size of the raster spot for the MARATHON experiment to two  
349 millimeters by two millimeters. This limit was installed has a safety concern for the  
350 tritium target.

351 The Hall A raster system consists of four dipoles. Two dipoles produce magnetic  
352 fields in the horizontal direction of the lab frame and two in the vertical. The upstream  
353 raster and downstream rasters include one vertical and one horizontal dipole. The  
354 relative change in position of the incoming electrons are controlled by the current  
355 supplied to the dipoles. In order to obtain the change in beam position due to the  
356 rasters, a calibration between the raster current and measured beam position were  
357 obtained.

358 The electron beam energy is located in many of the equations used in an electron  
359 scattering experiment. This can cause a noticeable increase in systematic error if the  
360 beam energy measurement is not made precisely. At JLAB for the MARATHON  
361 experiment, the beam energy was measured in two ways. In Hall A, the beam energy  
362 was measured by using the (e,e/p) method. On the beam line, 17 meters upstream  
363 from the target an ep scattering chamber is located. The beam was directed into the  
364 target containing a rotating 10-30  $\mu$ m thick tape of  $CH_2$ . The scattering angle of the  
365 electron and the recoil angle of the proton are used to determine the beam energy  
366 using equation 2.1. Where  $M_p$  is the mass of the proton and  $\theta_p, \theta_e$  are the scattered

<sup>367</sup> angle of the proton, electron respectively.

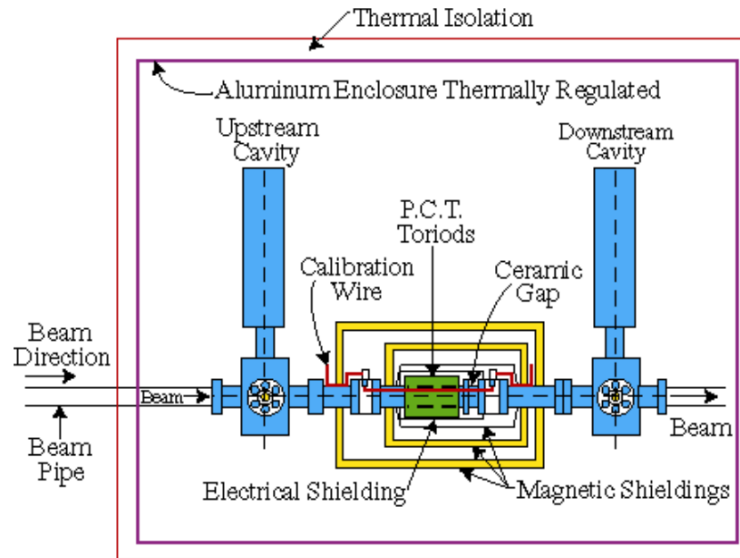
$$E = Mp \frac{\cos\theta_e + \frac{\sin\theta_e}{\tan\theta_p} - 1}{1 - \cos\theta_e} \quad (2.1)$$

<sup>368</sup> The beam energy was also measured using the ark measurement method [7]. This  
<sup>369</sup> method uses changes in beam position and precise measurements of the magnetic  
<sup>370</sup> fields around the beam line to determine the energy of the electron beam. The angle  
<sup>371</sup> at which the electrons are bent through is related to the momentum of the electrons,

$$p = k \frac{\int \vec{B} \cdot d\vec{l}}{\theta}. \quad (2.2)$$

<sup>372</sup> In equation 2.2, p is the momentum of the electrons,  $\theta$  is the bend angle, and  $\vec{B}$   
<sup>373</sup> is the magnetic field the electron experiences. Then using the momentum of the  
<sup>374</sup> electron, the energy of the beam can be extracted. The error on the beam energy  
<sup>375</sup> measurement is  $\delta E/E \approx 2 * 10^{-4}$  [22, 7]. The MARATHON experiment used both  
<sup>376</sup> methods to accurately determine the electron beam energy.

**Figure 2.6:** Hall A Current Monitor components [4].



377 The main process of measuring the scattering yield for a calculation of a cross  
378 section looks at finding the ratio of the number of electrons scattered to the number  
379 of electrons sent. In order to accurately determine the number of electrons sent to  
380 scatter with our target system, Hall A use a highly accurate and non-invasive beam  
381 current monitor(BCM). The Hall A BCM has an absolute accuracy of 0.2 percent  
382 as long as the current is between 1 and 180  $\mu$ A. The BCM used in Hall A consists of  
383 three main components: a Parametric Current Transformer (PCT) and two pill box  
384 cavities. Figure 2.6 shows the components in the Hall A BCM. The BCM produces  
385 an RF signal that is proportional to the beam current. An 10 kHz down converter,  
386 RMS-to-DC converter, voltage-to-Frequency converter, and a scaler are used to inject  
387 the current signal into the Hall A DAQ. Proportionality constants are determined in  
388 the calibration process to correctly integrate the charge for a given amount of beam  
389 current[4]. Continue after the initial beam line components, an electron will enter  
390 into the target chamber, housing the target system.

## 391 2.2 Target

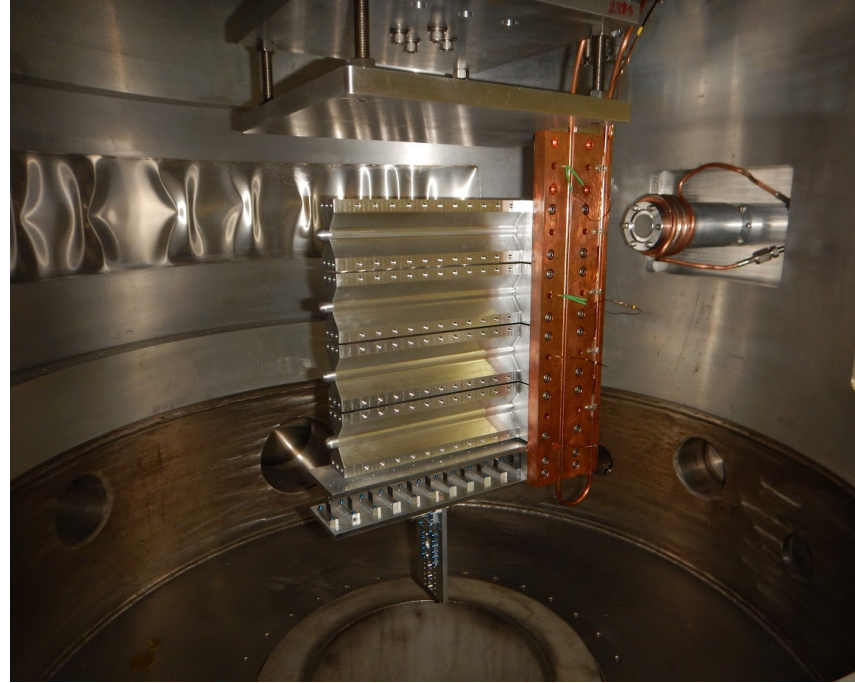
392 The Hall A Tritium Target(HATT) system was used for the Tritium run group of  
393 experiments. The HATT target chamber was repurposed from a previously used cryo-  
394 target chamber in order to reduce the financial cost of designing a new target chamber.  
395 The refurbishing of the cryo-target chamber consisted of adding in new safety features  
396 to prevent and mitigate a tritium leak. A 4 inch long collimator with an inner diameter  
397 of 0.4 inch was added inside of the target chamber but upstream of the target ladder  
398 to prevent the beam from striking the thin side wall of the aluminum cell. In case of  
399 a tritium leak in the target chamber, an exhaust system was installed to control the  
400 amount of tritium exposed to the Hall.[16] Figure 2.7 shows the HATT system with  
401 the target ladder in the home position and the scattering windows removed. A picture  
402 of the HATT ladder installed in the HATT system is shown if figure 2.7. The ladder  
403 contains both gaseous cells and solid targets. The MARATHON experiment had five

**Figure 2.7:** Target Images

(a) A image of the HATT. [11]



(b) Image of the Hall A Tritium Target Ladder. [11]



404 gas cells. The top four of the gas cells were filled with tritium, deuterium, hydrogen,  
405 and  $^3\text{helium}$ , from top to bottom respectively. Due to safety restricts the tritium  
406 cell was not installed until the HATT system could be closed. The bottom most  
407 cell was left empty, to complete end cap subtractions. The lower half of the target  
408 ladder contains the solid targets used during the MARATHON experiment. Listed  
409 from top to bottom, the solid targets used were a pair of thick aluminum foils, carbon  
410 multifoil, single carbon foil, and a carbon foil with a 2mm diameter hole. The thick  
411 Al foils were used to aid the target window background subtraction. The multifoil  
412 target also know has the optics target was used to calibrate the z-axis reconstruction  
413 of the optics matrix. The single carbon foil and carbon hole were used to calibrate  
414 the BPMs and rasters and to determine the off set of the central line of the detector.

## 415 2.3 High Resolution Spectrometers

416 Electrons that successfully scatter from the target may end up in either of the two  
417 HRSs(High Resolution Spectrometers). The HRSs were designed to detect charged  
418 particles with a high degree of precision. In order to achieve a high level of resolution  
419 in momentum and angle, the HRSs were designed with a magnet configuration of  
420  $QQD_nQ$  (quadrupole, quadrupole, dipole, and quadrupole). The vertical bending  
421 dipole provides the field required to transport the scattered particles through the  
422  $45^\circ$  bending angle to the detector hut. A drawing of an HRS can be seen in  
423 figure 2.8. The first quadrupole(Q1) focuses the incoming electrons in the vertical  
424 plane. The following two quadrupoles (Q2 and Q3 provide transverse focusing. This  
425 optical design allows the use of extended gas targets with no substantial loss in solid  
426 angle[1]. The spectrometers were designed to perform various functions which include:  
427 triggering the data acquisition system (DAQ) when certain requirements are met,  
428 gathering the position and direction of individual particles to reconstruct a track,  
429 provide precise timing information for time of flight calculations, and identify many  
430 different particle types that pass through the detector system. In order for both  
431 the Left HRS (LHRS) and Right HRS (RHRS) to complete the required task, they  
432 contain a myriad of detectors. The HRSs use drift chambers, scintillators, cerenkov  
433 detectors, and shower calorimeters. Both the Left and Right HRSs contain two planes  
434 of scintillators to function has the main trigger for the detector package. The vertical  
435 drift chambers (VDC) that lay at the front of the detector in conjunction with the  
436 Shower that lies in the back of the detector provide information for reconstructing the  
437 particle tracks and precise timing. Particles are identified by the cerenkov, shower  
438 calorimeters, and pion rejectors that are contained in the left or right HRS. The  
439 layout of the individual detectors that make up the left and right detector package  
440 are shown in figure 2.9 [1].

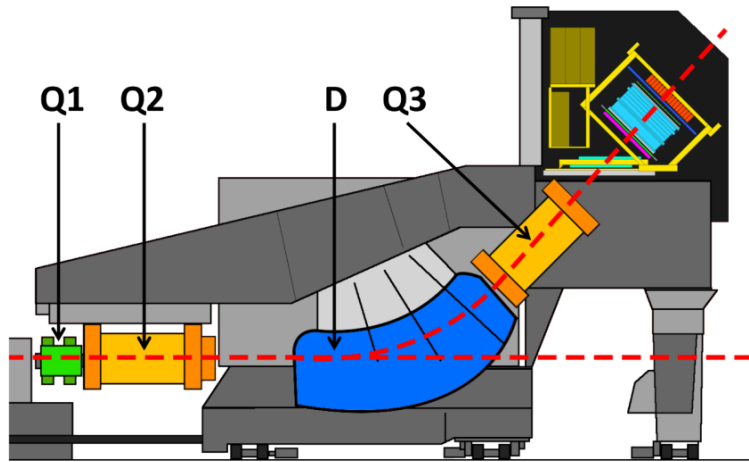


**Figure 2.8:** A side view of a HRS [1].

### 441 2.3.1 Vertical Drift Chambers

442 Each of the spectrometers housed in Hall A contains a vertical drift chamber(VDC).  
 443 Each VDC contains two planes of crossing sense wires. Shown in figure 2.10, the two  
 444 planes of the VDC lie a distance of 0.335m apart [6]. The lower plane of the VDC  
 445 is positioned at the approximate focal plane of the HRS and lies in the horizontal  
 446 plane of the Hall A coordinate system. The sense wires located in the VDCs cross  
 447 orthogonally. They are offset by  $45^\circ$  in respect to the dispersive and non-dispersive  
 448 directions.

449 [6]

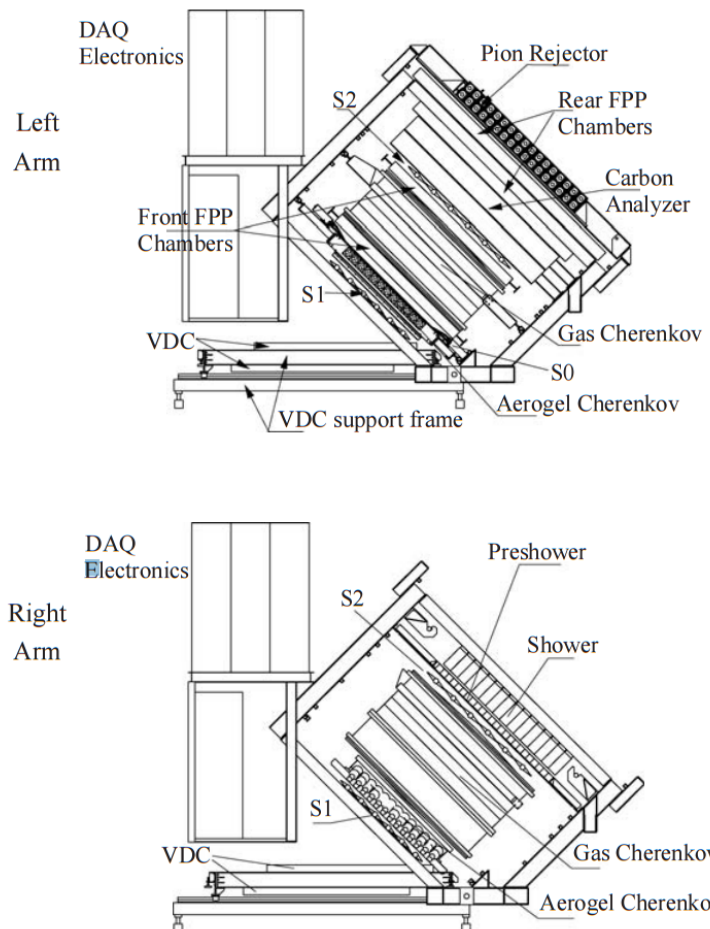


**Figure 2.9:** A view of both the left (top) and right (bottom) detector stacks inside the left and right HRS [1].

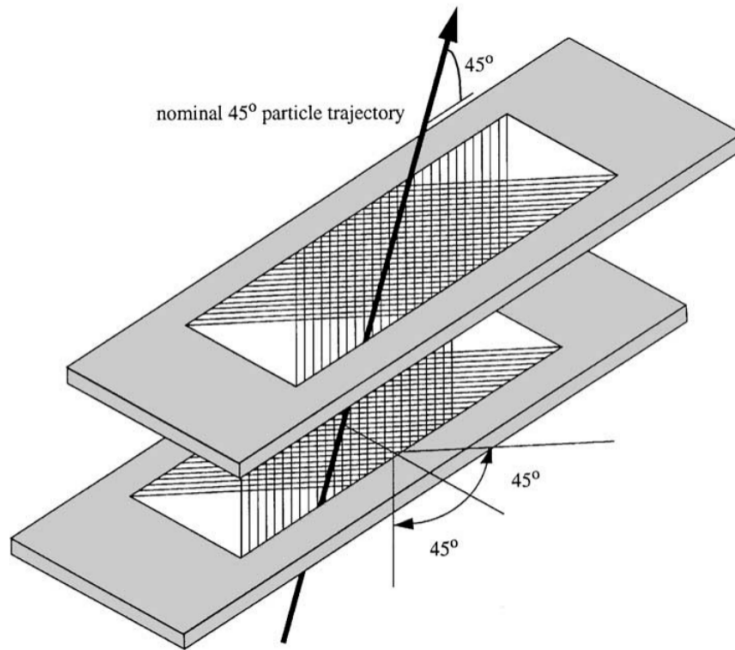


**Figure 2.10:** A sketch of the two VDC planes in the HRSs with a particle traveling through the detector at  $45^\circ$ .[6].

450    **2.3.2 Scintillators**

451    **2.3.3 Cherenkov**

452    **2.3.4 Shower Calorimeter**

453    **2.3.5 Pion Rejector**

454    **2.3.6 FPP Chambers**

455    **2.4 Trigger Setup**

456    **2.5 DAQ - Data Acquisition System**

457    **2.6 Kinematic Settings**

458 **Chapter 3**

459 **Calibration**

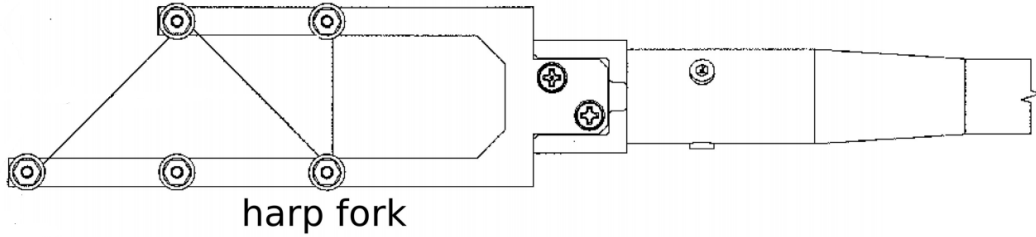
460 The information provided by the detectors originate through small changes in  
461 current and voltage sent through the DAQ electronics. These signals are transformed  
462 into useful information through calibration constants. The beam line elements and the  
463 individual detector components were calibrate to supply highly precise and accurate  
464 data.

465 **3.1 Beam Line**

466 The BPM signal coefficients are determined by a twiddle measurement. An RF  
467 module attached to the BPM antennas is used to pass a signal out of each of the  
468 antennas, one at a time. This will allow the determination of the conversion factor  
469 for the BPM signal to relative beam position. Two harps were used to provide  
470 the absolute measurement required for calibrating the BPMs. Figure 3.1 contains a  
471 drawing of the harps used in Hall A. The harps were moved into the beam line when  
472 calibration data is needed, but must be moved out for the production of experimental  
473 data because the harp wires are intrusive to the beam operation. The harp forks are  
474 aligned perpendicular to the beam line, to allow the harps to be moved in and out of  
475 the beam line. Three different wires are used to determine the horizontal and vertical  
476 position of the beam. Each wire has one of three orientations: vertical, sloped down

477 or sloped up. The two sloped wires are angled at 45° relative to the wire frame. As  
 478 the harp fork is moved into the beam, the wires receive a signal as the beam interacts  
 479 with the wires. The two sloped wires are used together to determine the vertical  
 480 position of the beam. The vertical wire is used to determine the horizontal position  
 481 of the beam [19, 23].

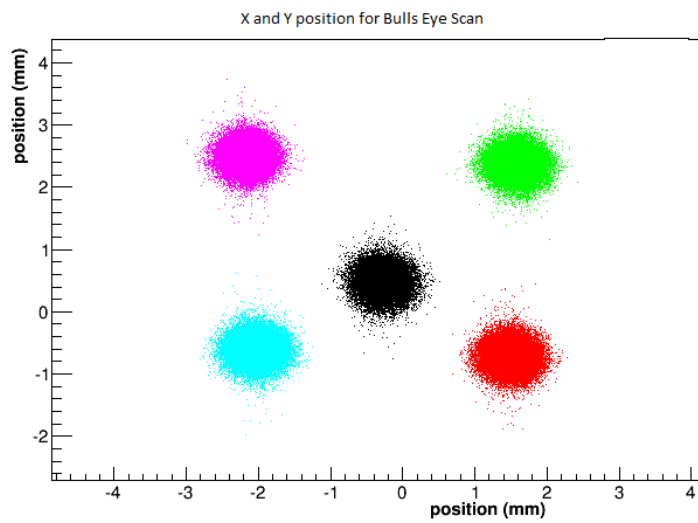
**Figure 3.1:** A schematic layout of a harp fork [23]



482 The location of the wires on the harp frame and the position of the harp fork  
 483 were used to calculate the absolute beam position. The BPM calibration coefficients  
 484 were determined by using a bulls eye scan, figure 3.2 shows an example of the five  
 485 positions used to calculate the BPM calibration coefficients. The harp scan results  
 486 are substituted into equation 3.1 for the X and Y positions. Using all five points and  
 487 an  $R^2$  regression technique, the coefficients can be determined with great accuracy.  
 488 These highly accurate BPMs were crucial in reducing systematic error in the final  
 489 results obtained from this experiment.

$$\begin{pmatrix} X_{position} \\ Y_{position} \end{pmatrix} = \begin{pmatrix} C(0, 0) & C(0, 1) \\ C(0, 0) & C(0, 1) \end{pmatrix} * \begin{pmatrix} X_{BPM} \\ Y_{BPM} \end{pmatrix} + \begin{pmatrix} X_{offset} \\ Y_{offset} \end{pmatrix} \quad (3.1)$$

**Figure 3.2:** The X and Y position for a Bulls eye scan for BPM calibration.



490 Chapter 4

491 Data Analysis

<sub>492</sub> Chapter 5

<sub>493</sub> Results

494 **Chapter 6**

495 **Simulation**

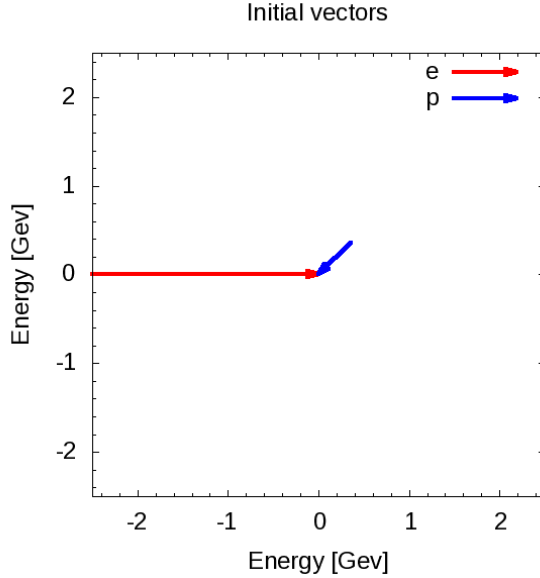
496 Nuclei are systems of nucleons that interact strongly. The characteristic scale for the  
497 nucleons momentum is approximately the Fermi momentum,  $k_F \approx 200 - 270 \text{ MeV}/c$   
498 [9]. However because of the strongly repulsive nature of the nucleon-nucleon  
499 interaction at short distances prevents two nucleons from laying in close proximately  
500 to each other. This strong interaction demands the presence of high-momentum  
501 components in the nuclear ground state wave function. A simulation was designed  
502 to phenomenologically study the effect of these high-momentum components on the  
503 nuclear EMC effect. This program was designed in two phases. The first phase used  
504 simple elastic scattering and a single value for the targets momentum to investigate  
505 overall effect of different target momentum on the yield in bins of  $x_B$ . The second  
506 phase of the simulation was created to lay out the effect of using different momentum  
507 distributions on the yield for the EMC effect region of  $x_B$ , 0.3 to 0.7.

508 **6.1 Investigation**

509 This simulation phenomenologically investigates the effect of a moving target on the  
510 EMC effect by scattering a beam of electrons off of a moving proton. The target  
511 protons are comprised of a directional vector of  $0^\circ$  to  $360^\circ$  in respect to the incoming  
512 electron beam and a momentum between 0 and 1 GeV/c. Figure 6.1 contains a

513 possible event for the simulation. The electron approaches with 2.5 GeV of energy  
514 and collides with a proton moving with a momentum of 0.5 GeV/c with an angle of  
45° in respect to the electron trajectory.

**Figure 6.1:** Example of the electron beam(red) with a energy of 2.5 GeV and the proton(blue) with angle of 45° in respect to the electron and with a momentum of 0.5 GeV/c.



515  
516     Using conservation of momentum and conservation of energy in elastic collisions,  
517     this simulation calculates the final state of the electron and proton after the scattering  
518     event by randomly selecting a scattered direction for the electron. The vector  
519     representation of the scattered products are shown in figure 6.3a. In order to  
520     make these calculations systematic and to study cross sections models the simulation  
521     transform each event into the rest frame of the target before scattering.

## 522     6.2 Transformation

523     The Simulation completes a set of Lorentz invariant rotations and boost for each  
524     event to transform the lab frame of the electron and proton collision into the rest  
525     frame of the proton. First the simulation takes the initial proton and electron vectors

526 and rotates them to align the proton vector to the horizontal axis, shown in figure  
 527 6.2b. This rotation uses the angle between the proton and the electron defined as  $\lambda$ .  
 528 This allows for a straight forward calculations for the Lorentz factors  $\beta$  and  $\gamma$  and  
 529 to boost into the rest frame of the target proton, figure 6.2c. Once in the boosted  
 530 frame, the angle between the electron and the horizontal axis is defined as  $\delta$ . Right  
 531 before the simulation starts to calculate the scattered products, it completes one more  
 532 rotation to align the electron vector with the horizontal axis, figure 6.2d, to make the  
 533 scattering calculation systematic and unconditional.

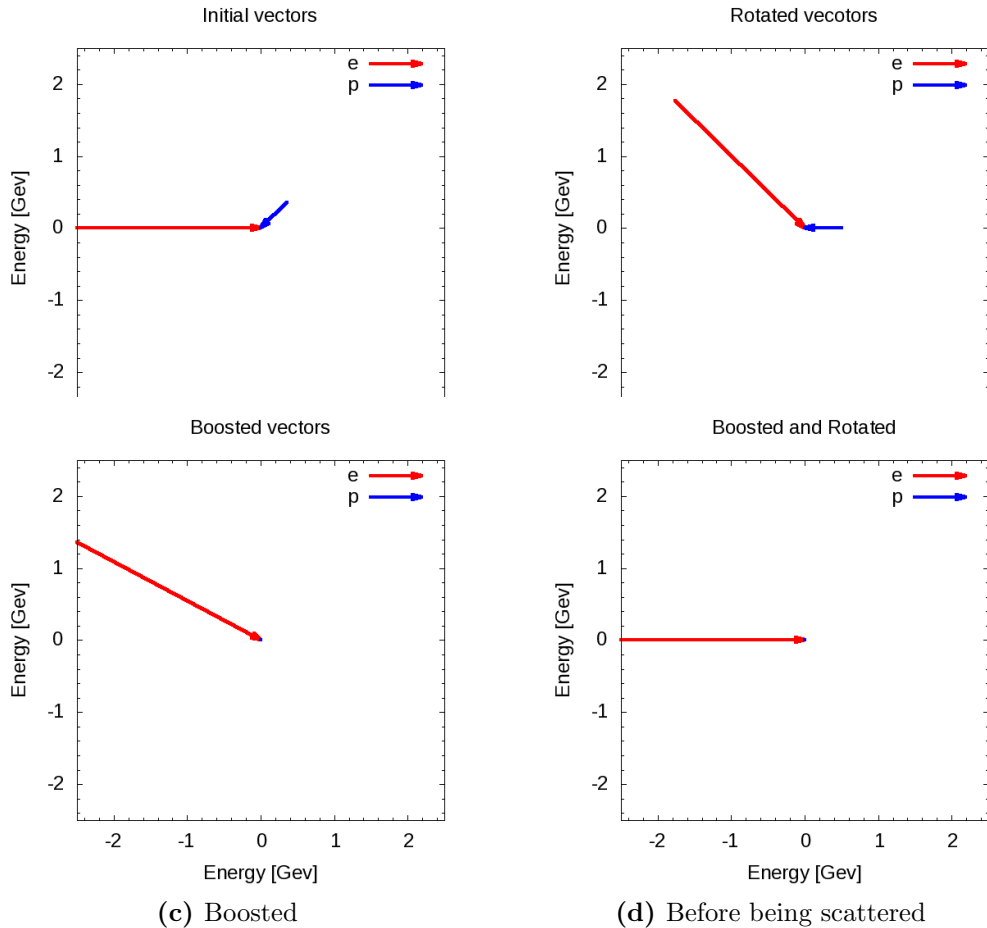


**Figure 6.2:** Vector representations of the momentum for the incoming electron(red) and target proton(blue) with units of GeV for each phase of their transformations before scattering.

534 In order to gain a more complete understanding of the scattering products, the  
535 program completes a set of transformations to move from the rest frame of the target  
536 proton to the beginning lab frame. After the simulation calculates the scattered  
537 products it begins to transform back by beginning with a rotation by the angle  $\delta$ ,  
538 figure 6.3b. Followed by the inverse of the previously used Lorentz boost. The  
539 last transformation, a rotation by  $\lambda$ , transforms the frame back into the lab frame.  
540 A proton vector and electron vector in the lab frame are the final products of the  
541 simulation. An image of the electron and proton vectors for each transformation can  
542 be found in figure 6.3. These vectors allow for calculation of kinematic variables such  
543 as Bjorken  $x$  and the four-momentum transfer ( $Q^2$ ). This simulation will complete  
544 these steps for many electron and proton combinations.

## 545 6.3 Results

546 This electron scattering simulation produced results for two stages. The firsts stage  
547 used a fix proton momentum for each run to compare the yield in bins of  $x_B$ . Figure  
548 6.4 shows the results for three different runs, each having a unique fixed proton  
549 momentum. The red histogram represents a run with a proton momentum of 0 Gev/c.  
550 The result is an elastic peak at  $x_B$  of one. The blue histogram contains the results  
551 having a fixed proton momentum of 0.25 GeV/c. Increasing the initial momentum  
552 of the proton spreads the events into two peaks. The scattering interactions that  
553 form the peak above 1  $x_B$  are produced by events were the proton's initial directional  
554 vector are orientated towards the electron. The events that produce an  $x_B$  below  
555 1 have a proton direction pointing away from the electron initially. Doubling the  
556 proton's initial momentum from 0.25 GeV to 0.50 GeV causes these peaks two spread  
557 out furtherer in  $x_B$ .

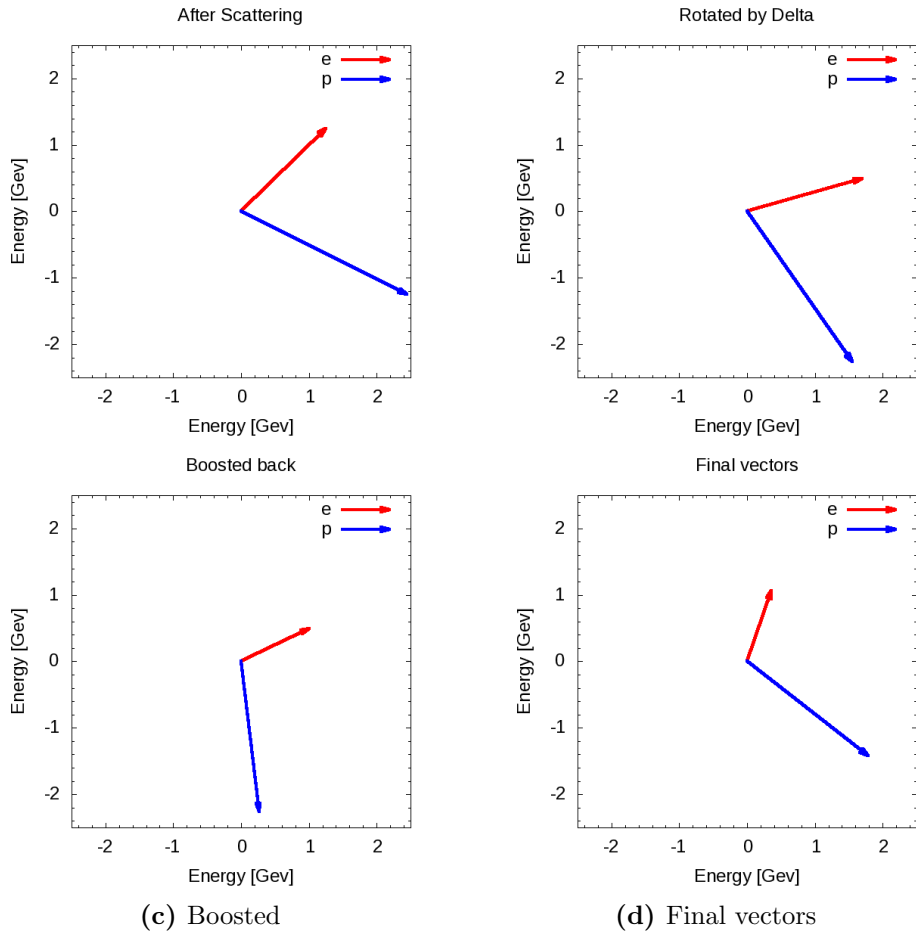
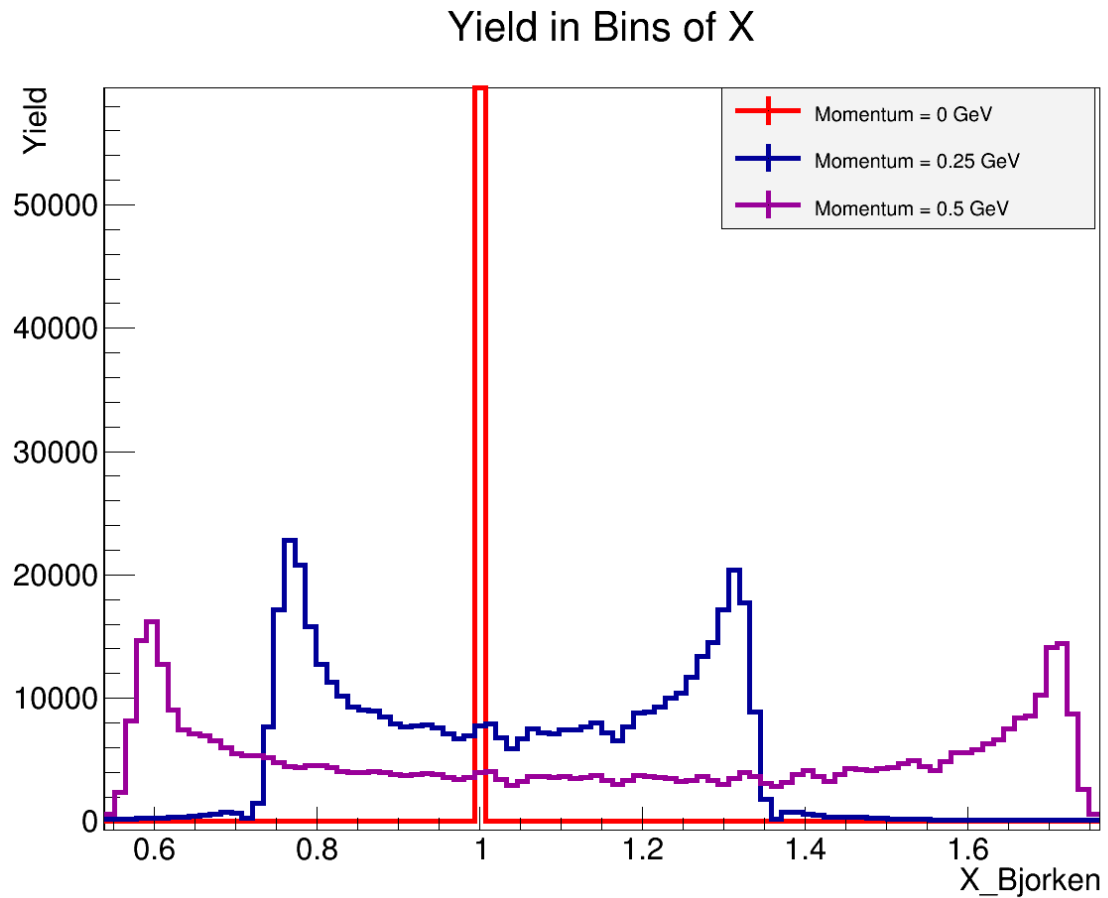


**Figure 6.3:** Vector representations of the momentum for the incoming electron(red) and target proton(blue) with units of GeV for each phase of their transformations after scattering).

**Figure 6.4:** Simulation results for fixed momentum protons. Three runs with unique proton momentum.



558 Chapter 7

559 Conclusion

# Bibliography

561

# Bibliography

- 562 [1] J. Alcorn et al. Basic Instrumentation for Hall A at Jefferson Lab. *Nucl. Instrum. Meth.*, A522:294–346, 2004. [vi](#), [11](#), [12](#), [13](#), [19](#), [20](#), [21](#)
- 564 [2] John Arrington, Aji Daniel, Donal Day, Nadia Fomin, Dave Gaskell, and Patricia Solvignon. A detailed study of the nuclear dependence of the EMC effect and short-range correlations. *Phys. Rev.*, C86:065204, 2012. [8](#)
- 566 [3] A. Daniel, J. Arrington, and D. Gaskell. Measurements of the EMC effect in few-body nuclei at large x. *AIP Conf. Proc.*, 1369:98–105, 2011. [9](#)
- 569 [4] J. Denard and J. Sahar. High accuracy beam current monitor system for cebaf’s hall a. Chicago, 2001. Particle Accelerator Conference. [vi](#), [16](#), [17](#)
- 571 [5] J. Edelmann, G. Piller, Norbert Kaiser, and W. Weise. Resonances and higher twist in polarized lepton nucleon scattering. *Nucl. Phys.*, A665:125–136, 2000. [8](#)
- 573 [6] K.G. Fissum et al. Vertical drift chambers for the hall a high-resolution spectrometers at jefferson lab. *Nuclear Instruments and Methods in Physics Research Section A: Accelerators, Spectrometers, Detectors and Associated Equipment*, 474(2):108 – 131, 2001. [vi](#), [20](#), [22](#)
- 577 [7] David J. Flay. *Measurements of the Neutron Longitudinal Spin Asymmetry A1n and Flavor Decomposition in the Valence Quark Region*. PhD thesis, Temple University, Philadelphia, PA, Aug 2014. [vi](#), [2](#), [3](#), [16](#)

- 580 [8] D.F. Geesaman, K Saito, and A Thomas. The nuclear emc effect. *Annual Review*  
581       *of Nuclear and Particle Science*, 45(1):337–390, 1995. [8](#)
- 582 [9] J. Gomez et al. Measurement of the A-dependence of deep inelastic electron  
583       scattering. *Phys. Rev.*, D49:4348–4372, 1994. [8, 28](#)
- 584 [10] D. Higinbotham. The emc effect still puzzles after 30 years - cern courier.  
585       <http://cerncourier.com/cws/article/cern/53091>, April 2013. (Visited on  
586       01/04/2016). [vi, 2, 7, 9](#)
- 587 [11] Doug Higinbotham. Target images, December 2017. [18](#)
- 588 [12] R Hofstadter. Nuclear and nucleon scattering of high-energy electrons. *Annual*  
589       *Review of Nuclear Science*, 7(1):231–316, 1957. [4](#)
- 590 [13] Henry W. Kendall. Deep inelastic scattering: Experiments on the proton and  
591       the observation of scaling. *Rev. Mod. Phys.*, 63:597–614, Jul 1991. [6](#)
- 592 [14] Simona Malace, David Gaskell, Douglas W. Higinbotham, and Ian Cloet. The  
593       Challenge of the EMC Effect: existing data and future directions. *Int. J. Mod.*  
594       *Phys.*, E23:1430013, 2014. [6](#)
- 595 [15] R. W. McAllister and R. Hofstadter. Elastic scattering of 188-mev electrons from  
596       the proton and the alpha particle. *Phys. Rev.*, 102:851–856, May 1956. [2](#)
- 597 [16] David Meekings. Hall a tritium target. Thomas Jefferson Lab, Virginia,  
598       engineering Report, 2017. [17](#)
- 599 [17] P R Norton. The emc effect. *Reports on Progress in Physics*, 66(8):1253, 2003.  
600       [vi, 8](#)
- 601 [18] Bogdan Povh, Klaus Rith, Christoph Scholz, and Frank Zetsche. *Particles and*  
602       *Nuclei: An Introduction to the Physical Concepts*. Springer, 2009. [1, 2, 4, 5, 6](#)

- 603 [19] Tom Powers, Lawrence Doolittle, Rok Ursic, and Jeffrey Wagner. Design,  
604 commissioning and operational results of wide dynamic range bpm switched  
605 electrode electronics. *AIP Conference Proceedings*, 390(1):257–265, 1997. [13](#),  
606 [24](#)
- 607 [20] J. Seely et al. New measurements of the european muon collaboration effect in  
608 very light nuclei. *Phys. Rev. Lett.*, 103:202301, Nov 2009. [2](#), [9](#)
- 609 [21] Richard E. Taylor. Deep inelastic scattering: The early years. *Rev. Mod. Phys.*,  
610 63:573–595, Jul 1991. [6](#)
- 611 [22] Hall A Tech. Ep method. [http://hallaweb.jlab.org/equipment/beam/  
612 energy/ep\\_web.html](http://hallaweb.jlab.org/equipment/beam/energy/ep_web.html). (Accessed on 06/28/2016). [16](#)
- 613 [23] Pengjia Zhu et al. Beam Position Reconstruction for the g2p Experiment in Hall  
614 A at Jefferson Lab. *Nucl. Instrum. Meth.*, A808:1–10, 2016. [vi](#), [13](#), [14](#), [15](#), [24](#)

# Appendix

615